

See discussions, stats, and author profiles for this publication at: <https://www.researchgate.net/publication/231650108>

Observation of Extra-High Depolarized Light Scattering Spectra from Gold Nanorods

ARTICLE in THE JOURNAL OF PHYSICAL CHEMISTRY C · AUGUST 2008

Impact Factor: 4.77 · DOI: 10.1021/jp802874x

CITATIONS

42

READS

78

3 AUTHORS:



Boris Khlebtsov

Russian Academy of Sciences

152 PUBLICATIONS 2,185 CITATIONS

SEE PROFILE



Vitaly Khanadeev

Russian Academy of Sciences

42 PUBLICATIONS 467 CITATIONS

SEE PROFILE



Nikolai G. Khlebtsov

Institute of Biochemistry and Physiology of...

229 PUBLICATIONS 4,812 CITATIONS

SEE PROFILE

Observation of Extra-High Depolarized Light Scattering Spectra from Gold Nanorods

Boris N. Khlebtsov,[†] Vitaly A. Khanadeev,[‡] and Nikolai G. Khlebtsov^{*,†,‡}

Institute of Biochemistry and Physiology of Plants and Microorganisms, Russian Academy of Sciences, 13 Prospekt Entuziastov, Saratov 410049, Russia, and Saratov State University, 83 Ulitsa Astrakhanskaya, Saratov 410026, Russia

Received: April 3, 2008; Revised Manuscript Received: June 11, 2008

We report on depolarized light scattering spectra from suspensions of gold nanorods in terms of the depolarized ratio I_{vh}/I_{vv} measured from 400 to 900 nm. For separated, highly monodisperse and highly monomorphic samples, we observed spectra with an unprecedented depolarization ratio with a resonance maximum of about 50% at wavelengths of 600–650 nm, below the long-wavelength 780 nm extinction peak. These unusual depolarization ratios are between 1/3 and 3/4 theoretical limits established for small dielectric and plasmon-resonant needles, respectively. Our measurements showed a strong correlation between the resonance depolarization ratio and the ratio of the long-wavelength to short-wavelength extinction resonances. Specifically, for standard seed-mediated-growth nanorods with a round-end-cylinder or a “dog-bone” shape morphology, the peak-extinction ratios were less than 3 and the resonance depolarization ratio was about 30–35%. The measured extinction and depolarization spectra are in excellent agreement with T-matrix simulations based on TEM data. For silver nanorods, our T-matrix simulations predict multiple-peak depolarization spectra and unique depolarization ratios exceeding the upper dipolar limit (3/4) because of multiple depolarization contributions.

1. Introduction

The anisotropic optical properties of metal nanoparticles and nanostructures are of great interest for potential biological,¹ chemical,² and medical applications.³ Recent development of nanoparticle-pattern technologies stimulated interest in studying the anisotropic optical properties of artificial 2D arrays with controlled structure parameters.⁴ Here, we focus on the anisotropic properties of nanoparticle suspensions.

If colloidal nonspherical particles are preferentially oriented by an external field, the suspension exhibits anisotropic properties such as dichroism, birefringence, and orientation-dependent variations in turbidity and in light scattering.⁵ Moreover, even for randomly oriented particles, there remain some principal differences between light scattering from nanospheres and that from nanorods. Indeed, when randomly oriented nonspherical particles are illuminated by linearly polarized light, the cross-polarized scattering intensity occurs,^{6,7} whereas for spheres this quantity equals zero, as was established in the pioneering studies by Rayleigh.⁸

The cross-polarized scattered intensity I_{vh} can be characterized by the depolarization ratio $\Delta_{vh} = I_{vh}/I_{vv}$, where the subscripts “v” and “h” stand for vertical and horizontal polarization with respect to the scattering plane (Figure 1). According to the theory of light scattering by small particles,^{6,7} the maximal value of the depolarization ratio Δ_{vh} cannot exceed 1/3 and 1/8 for dielectric rods and disks with positive values of the real and imaginary parts of dielectric permeability. However, it has recently been shown^{9,10} that the dielectric limit 1/3 does not hold for plasmon-resonant nanorods whose theoretical depolarization limit equals 3/4 (the same conclusion has also been confirmed in ref 11).

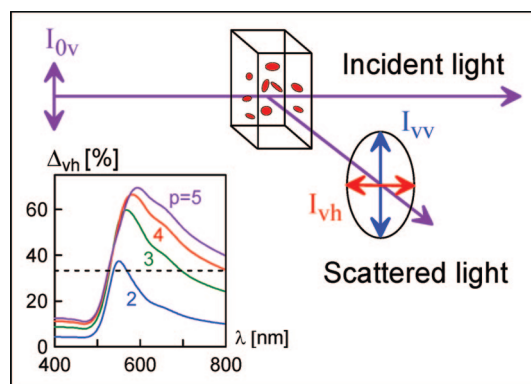


Figure 1. Scheme for illumination and observation of depolarized light scattering. The inset shows the theoretical depolarized ratio spectra calculated by the T-matrix method for randomly oriented gold nanorods in water. The numbers near the curves designate the particle aspect ratio from 2 to 5 for rods with a thickness of 15 nm. Throughout the paper, we used an s-cylinder model^{9,10} (cylinders with semispherical ends, the diameter $d = 2b$, the length $L = 2a$, and the aspect ratio $p = a/b$).

Our exact T-matrix simulations for gold nanorods^{9,10} and approximate dipole calculations for silver spheroids¹¹ showed that (1) the maxima of the depolarization-ratio spectra are shifted to the short wavelengths, compared with the dominant longitudinal extinction resonance, and that (2) the depolarization ratio becomes greater than 1/3 in the red part of the depolarization spectrum even at moderate axial ratios $p = a/b > 2$ (Figure 1, inset).

However, the only experimental verification of the inequality $\Delta_{vh} > 1/3$ has been provided for a single He–Ne laser wavelength.⁹ As far as we are aware, no experimental observation of depolarized light scattering spectra with resonance values $\Delta_{vh} > 1/3$ has ever been reported. In addition, there have been no accurate comparisons of measured and exactly calculated

* To whom correspondence should be addressed. E-mail: khlebtsov@ibppm.sgu.ru.

[†] Russian Academy of Sciences.

[‡] Saratov State University.

depolarization spectra from gold nanorods. The primary goal of this work was to fill these gaps.

The spectral properties of the depolarized ratio may find some interesting applications in various fields. First, it is well-known¹² that strong correlations exist between the particle shape morphology and the depolarized light scattering properties. However, in the case of dielectric (especially biological) particles, depolarized scattering is too weak to be useful in routine laboratory practice. By contrast, plasmon-resonant metal nanoparticles demonstrate extraordinary depolarization values, greater than 10% even for moderate aspect ratios. Therefore, the appearance of depolarized light scattering is quite an informative test for deviation of ensemble particles from the spherical shape. Another possible application of Δ_{vh} measurements may be related to chemical and biological sensing based on the assembly of spherical particles. Consider spherical gold particles whose surface is functionalized with a biomolecular probe. Such an ensemble gives zero depolarization. However, if an interaction with target molecules forms a particle duplex or more complex clusters, depolarized light scattering will indicate the molecular binding events. Finally, depolarized light scattering may be useful in the dark-field microscopy of living cells. Specifically, for cross-polarized optical measurements, it may be possible to exclude a strong copolarized component in tracking individual receptors within single living cells by using conjugates of molecular probes with strongly depolarizing nanoparticle reporters (e.g., nanorods or stellated particles³).

2. Experimental Section

2.1. Sample Preparation. For sample preparation, the following reagents were used: tetrachloroauric acid (TCAA) (Aldrich), cetyltrimethylammonium bromide (CTAB) (Acros and Fluka), sodium borohydride (Serva, Germany), silver nitrate, ascorbic acid, 25% aqua ammonia (Reachim Co., Russia), tetraethyl orthosilicate (TEOS, Aldrich), absolute ethanol (ET0016, Scharlau Chem. S.A., Spain), and tridistilled water. All glassware that was used was cleaned with 3:1 HCl/HNO₃ and was rinsed thoroughly in H₂O before use.

Au nanorods were synthesized according to the seed-mediated-growth method,¹³ with minor modifications concerning the concentrations of some reagents and reaction protocols¹⁴ and 2¹⁵ (see below). Two samples, NR-780 and NR-670 (designated according to the resonance wavelength), were prepared by protocol 1 with Fluka and Acros CTAB, respectively. In agreement with a recent report by Smith and Korgel,¹⁶ we also noted that the yield and quality of gold nanorods depended on the CTAB used. The best results were obtained with Fluka CTAB. NR-740 particles were fabricated by protocol 2 with Acros CTAB.

In protocol 1, seed gold particles were formed by adding aqueous sodium borohydride (0.01 M, 1 mL) to a mixed aqueous solution of Fluka CTAB (0.1 M, 1 mL) and TCAA (0.01 M, 0.25 mL). NR-780 particles were fabricated by adding 0.018 mL of the gold seed solution to a growth solution of CTAB (0.10 M, 9.50 mL), silver nitrate (0.004 M, 0.25 mL), TCAA (0.01 M, 0.5 mL), and ascorbic acid (0.08 M, 0.1 mL). The nanorods were allowed to grow overnight without stirring at 24 °C.

For NR-670 particles, the same protocol was used except that Fluka CTAB was replaced with Acros CTAB. The following volumes were used for the growth solution: 0.012 mL of gold seeds and 0.15 mL of silver nitrate.

NR-740 particles were fabricated by protocol 2 with Acros CTAB. In protocol 2, seed gold particles were formed by adding

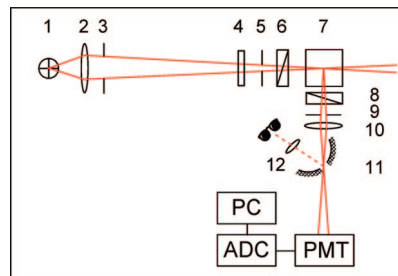


Figure 2. Experimental setup. The numbers represent a halogen lamp (1), achromatic lenses (2, 10, 12), iris diaphragms (3, 5, 9), interference filters (4), a four-sided 1 cm rectangular cuvette (7), polarization prisms (6, 8), and a spherical mirror with a pinhole diaphragm (11). The symbols represent the photomultiplier (PMT), the analog-to-digital converter (ADC, L-Card Ltd., Russia), and the personal computer (PC).

aqueous sodium borohydride (0.01 M, 0.3 mL) dropwise to a stirred (500 rpm) aqueous solution of Acros CTAB (0.02 M, 5 mL) and TCCA (0.03 M, 0.083 mL). NR-740 particles were fabricated by adding 0.012 mL of the gold seed solution to a growth solution of Acros CTAB (0.2 M, 9.5 mL), silver nitrate (0.01 M, 0.1 mL), TCAA (0.03 M, 0.166 mL), and ascorbic acid (0.1 M, 0.1 mL). The nanorods were stirred (500 rpm) for 60 min at 30 °C.

For separation of nanorods,¹⁰ the following solutions were prepared: $n[\text{g}]$ glycerol + $m[\text{g}]$ 100 mM CTAB (Acros), where $n = 1, 2, \dots, 5$ and $m = 9, 8, \dots, 5$. A 10 mL nanorod solution was centrifuged for 7 min at 13 500g. Then, 9.6 mL of supernatant liquid was removed, and the sediment was layered over a stepwise density gradient of glycerol (from 50 to 10%; step, 10%) with 2 mL for each step of density, in a rotary tube with a total volume of 15 mL. These tubes were centrifuged (30 min, 4000g), and the upper part of the first layer was used for further experiments.

To test the depolarization setup, we used 137 nm polystyrene latex (Metachem Diagnostics, Ltd., U.K.), 114 and 160 nm silica nanoparticles, and 15 and 50 nm colloidal gold particles. The silica nanospheres were fabricated by Stöber's¹⁷ method as described in ref 18. Gold nanospheres were prepared by the citrate reduction method, as described in ref 9. The particle size distributions were obtained from dynamic light scattering (DLS) and TEM data.

2.2. Sample Characterization and Optical Measurements. DLS measurements were carried out with a PhotoCorr FC instrument (Photo Corr Inc., Russia). TEM characterization was made with a Libra-120 transmission electron microscope (Carl Zeiss, Germany). The extinction spectra were recorded with a UV-vis Specord BS-250 (Analytik Jena, Germany) and a Specord M-40 (Carl Zeiss, Germany) spectrophotometer.

Depolarized light scattering spectra $\Delta_{\text{vh}}(\lambda)$ were measured with the homemade setup shown in Figure 2. The light beam from a halogen lamp (1) travels through the interference filter (4) and the polarization prism (6) and focuses near the center of a four-sided quartz cuvette (7). The scattered light is analyzed by using the polarization prism (8), the photomultiplier (PMT), the analog-to-digital converter (ADC), and PC software. A spherical mirror (11) with a central pinhole and with a lens (12) allows visual control of scattering volume imaging with respect to the pinhole. Depending on the scattering intensity, which is determined by the pinhole diameter, the particle concentration, and the scattering cross section, the setup can operate in an analog or a photon-counting mode. Some experimental details concerning the depolarization setup can be found in the Supporting Information.

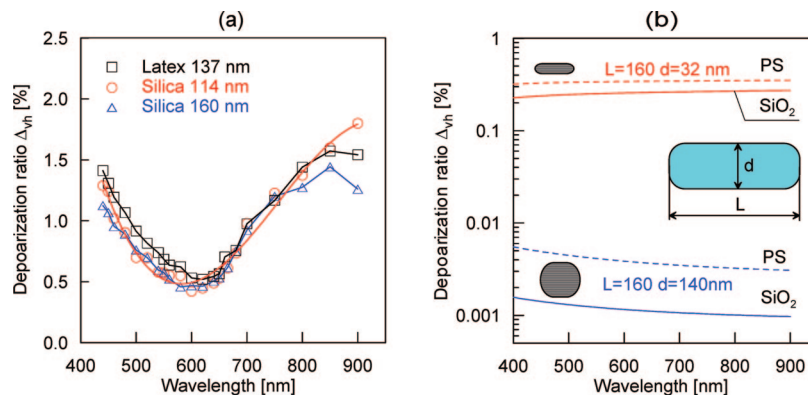


Figure 3. (a) Experimental depolarization spectra of 137 nm polystyrene latex, 114 and 160 nm silica nanospheres. (b) T-matrix calculations for randomly oriented polystyrene (PS) and silica s-cylinders in water with length $L = 160$ nm and diameters $d = 32$ and 140 nm.

A typical measurement protocol was as follows. First, for a given wavelength, the photocurrents I_{vh}^0 and I_{vv}^0 were measured for the solvent (in our case, water). Then, similar quantities (I_{vh} and I_{vv}) were measured for a sample. Finally, the depolarization ratio was calculated by $\Delta_{vh} = (I_{vh} - I_{vh}^0)/(I_{vv} - I_{vv}^0)$. Note that the dark-current contribution is excluded by this procedure.

3. Results and Discussion

3.1. Testing the Depolarization Setup. In general, depolarization measurements can be affected by unwanted depolarized contributions from the optical elements, the polarization-dependent response of PMT, the nonideality of polarization prisms, and so on. Therefore, we first checked the accuracy of our setup by using several benchmark samples, such as 137 nm polystyrene latex, 114 and 160 nm silica spheres, and 15 and 50 nm colloidal gold suspensions. Figure 3a shows the depolarization spectra of silica and polystyrene particles. In spite of some insignificant variations, all three spectra demonstrate very close behaviors with 1–1.5% maxima near 400 and 900 nm and 0.5% minima near 600 nm. To elucidate the origin of the measured spectra, we performed a set of T-matrix calculations for silica and polystyrene s-cylinders randomly oriented in water. The aspect ratio was varied from 1 (ideal spheres) to 5. For illustration, Figure 3b shows the calculated depolarization spectra for dielectric particles with a small deviation from sphericity, when the aspect ratio $p = L/d$ equals $16/14 = 1.14$. Clearly, the calculated values of $\Delta_{vh} \leq 0.01\%$ are too small to be considered a possible origin of the experimental spectra in Figure 3a. Moreover, our calculations for dielectric polystyrene and silica rods ($p = 5$) rule out any explanation for the Figure 3a spectra by using single-particle dielectric models. Thus, we attribute the depolarization spectra in Figure 3a to the instrumental contribution that determines the upper limit of the absolute systematic errors of our experimental setup. These estimations should be taken into account in the discussion of experimental data for gold nanorods.

The scattering intensity from 15 nm gold particles was too small to be measured correctly. In fact, the measured depolarization ratios were within the range defined by the instrumental curves shown in Figure 3a. Therefore, we do not present a depolarization spectrum for 15 nm gold particles because of significant instrumental errors. For 50 nm gold particles, the scattering intensity was quite appreciable to allow depolarization spectrum measurements to be made with admissible accuracy (Figure 4). Comparison with the T-matrix calculations for various input geometrical parameters showed that the calculated spectra were significantly narrower than the experimental curves.

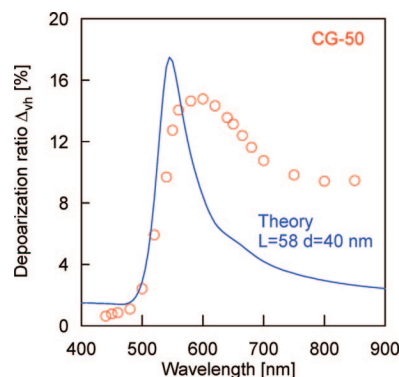


Figure 4. Experimental depolarization spectrum of 50 nm gold particles (points) and a theoretical curve for a water suspension of randomly oriented gold s-cylinders ($L = 58$ nm, $d = 40$ nm).

For illustration, we provide in Figure 4 a calculated curve for a water suspension of randomly oriented gold s-cylinders with a 58 nm length and a 40 nm diameter. Thus, a simple monosize and monoshape model is not consistent with the experimental depolarization spectrum. Below, in discussing the data for gold nanorods, we shall consider more sophisticated models that account for the aspect-ratio distribution and for the presence of byproduct particles.

To conclude this section, we shortly discuss the particle concentration effects. There are two important physical points to be made. First, at “moderate” concentrations (say, if the optical densities of solutions in a 1 cm cuvette are less than 1), there may be re-extinction of the scattered light. As the extinction is strongly spectrally dependent, this re-extinction could result in a significant distortion of the experimental depolarization spectra. This problem occurs, e.g., during elastic-scattering-spectra measurements, for a strongly absorbing colloidal gold solution. In principle, secondary extinction can be taken into account by using special measurement or correction schemes, as described in ref 19. Fortunately, in the case of depolarization spectra, there is no need for such a correction because the quantity of interest, Δ_{vh} , is defined as the ratio between the scattered intensities. Clearly, the correction factors will be eliminated from the final quantity.

The second issue is related to the change in scattered-light polarization because of multiple scattering events. It is well-known that multiple scattering may result in a significant change in the initial Stokes vector²⁰ within a multiple scattering medium. To exclude these effects, we used diluted solutions with resonance optical densities of less than 1. In addition, we checked the absence of significant differences between the

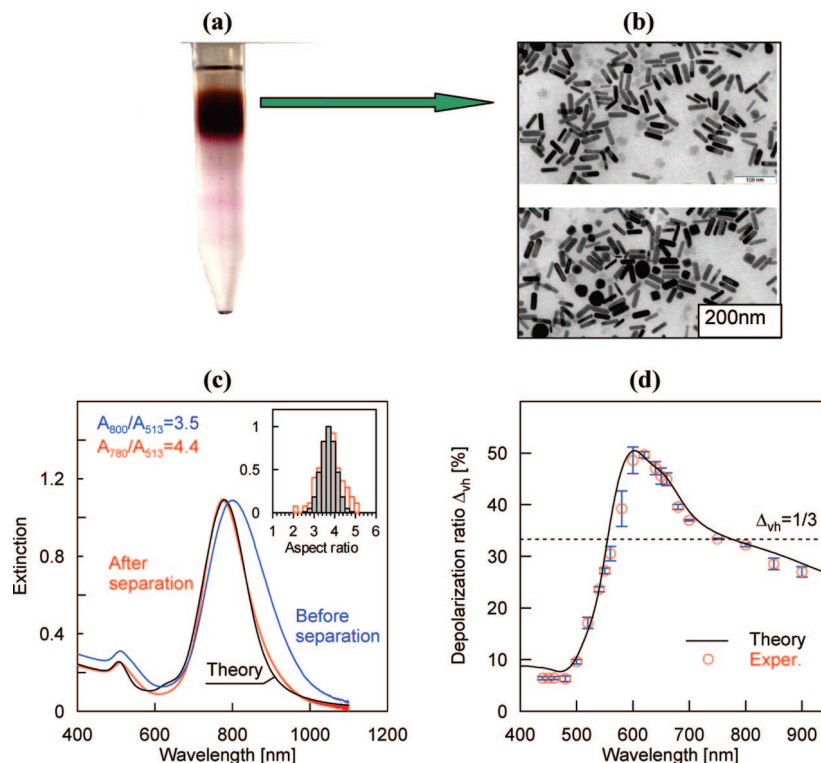


Figure 5. (a) Separation of the NR-780 sample in a stepwise glycerol gradient. (b) TEM image of the upper portion of the first major fraction from the separation tube (top) and the same sample before separation (bottom). (c) Extinction spectra of the NR-780 sample before and after separation, together with T-matrix calculations based on best-fitting data ($p_{\text{av}} = 3.7$, $\sigma = 0.1$, $W_b = 0.06$). The inset shows a comparison of a TEM aspect distribution (light columns) with a normal best-fitting distribution (dark columns) for the same sample taken after separation. (d) Experimental and simulated depolarization spectra. The error bars correspond to three independent runs, with analog and photon-counting data included. The dashed line shows the dielectric-needle limit $1/3$.

depolarization spectra measured for the initial sample and after 2-fold dilution. In any case, the above testing experiments (Figure 3) gave the upper limits for the total experimental errors, which also might have included the multiple scattering contributions.

3.2. Optical and TEM Data for NR-780 Gold Nanorods.

The main difficulty in observation of high depolarization ratios is related to particle heterogeneity. That is why all previously reported depolarization ratios were less than 30–35% for gold nanorods^{9,10} and less than 10–25% for silver colloids.^{21,22} This can easily be understood from simple physical arguments. The depolarization resonance band is shifted to the short wavelengths, where the scattering intensity from rods is strongly decreased. On the other hand, undesired byproduct particles may give an appreciable contribution to copolarized, but not cross-polarized, intensity, leading to a significant decrease in the measured depolarization ratio, as compared with the theoretical ratios calculated for monosized and monoshaped particles. Thus, a separation procedure is needed to improve the quality of as-prepared samples.

Recently, Hanauer et al.²³ demonstrated the separation by agarose gel electrophoresis of gold and silver nanoparticles according to their size and shape. However, this method is not suitable for preparative goals, and the quality of separated-nanoparticle spectra²³ seems insufficient for our purposes. Specifically, we found that the depolarization ratios $\Delta_{\text{vh}} > 1/3$ can only be achieved with samples possessing the extinction peak ratio $A_2/A_1 > 3-4$, where the subscripts 1 and 2 stand for the short- and long-wavelength resonances, respectively. To this end, we applied the sedimentation protocol described in section 2.1 and in ref 10.

Figure 5a shows the separation profile for an NR-780 sample. The top dark-red band corresponds to the major nanorod fraction, whereas the lower red-colored bands represent minor byproduct particles, clearly seen in the TEM images before separation (Figure 5b, bottom panel). For depolarization experiments, only the upper portion of the rod bands was taken. However, even with this preparative caution exercised, the TEM images (Figure 5b, top panel) reveal the presence of a remaining minor fraction of particles having a round-cube or a spherical shape. Such particles have been observed previously,²⁴ and they could not be removed by the separation procedure used. Nevertheless, a direct comparison of the TEM images (Figure 5b, top and bottom) unambiguously shows that most byproduct particles were eliminated by separation.

The extinction spectra before and after separation (Figure 5c) differ in both the major resonance location (800 nm before and 780 nm after separation) and the resonance peak A_2/A_1 ratio, which increases from 3.5 to 4.4. From our experimental experience, we could expect that samples with such an outstanding peak ratio should exhibit remarkable depolarization properties.

Indeed, the depolarization spectrum in Figure 5d demonstrates an evident resonance band between 550–750 nm with an unprecedented maximal depolarization ratio of about 50%. The error bars represent standard deviations for three independent experimental runs. Furthermore, to exclude possible experimental errors caused by instrumental depolarization, deviations from the 90° observation angle, and so on, we ran an independent experiment with the smallest pinhole diaphragm (0.1 mm) and repeated all measurements in the photon-counting mode. The results were the same as those shown in Figure 5d. Thus, Figure 5d can be considered the first strong evidence for

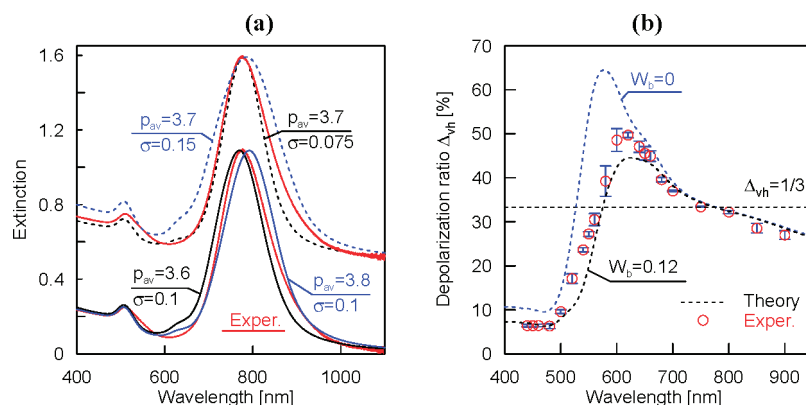


Figure 6. Testing the best-fitting parameters of aspect-ratio distributions. (a) Comparison of the experimental and simulated extinction spectra at a constant best-fitting dispersion of $\sigma = 0.1$ and at a constant best-fitting average value of $p_{av} = 3.7$ (the plots are shifted to 0.5 for convenience). Clearly, the average value and dispersion errors are less than 0.1 and 0.05, respectively. (b) Comparison of the measured and simulated depolarization spectra calculated without byproduct particles ($W_b = 0$) and with a weight parameter of $W_b = 2W_b^{\text{best fit}} = 0.12$. Both simulations result in poor agreement with the experimental spectra, in comparison with the best-fitting $W_b = 0.06$ (Figure 5d).

resonance depolarized light scattering with extra-high ratios exceeding the dielectric-needle limit⁹ of 1/3.

In general, the spectrum profile agrees with theoretical simulations based on the simplest monodisperse and monoshape particle model (see ref 9 and the inset in Figure 1). We now proceed to a more detailed comparison between the experimental extinction and depolarization spectra and the theoretical simulations based on TEM data. Note that only the separated sample will be considered further because the initial solution contained a substantial amount of byproduct particles. Our goal is twofold: (1) To compare the measured and simulated extinction and depolarization spectra. (2) To compare the TEM and optically fitted shape distributions for the same separated sample and to evaluate the accuracy of nanorods' geometrical parameters generated by the optical data. Here, we apply a modified Eustis and El-Sayed²⁵ approach, which can be summarized as follows.

The experimental broadened extinction and depolarization spectra are fitted with a collection of homogeneously broadened spectra based on T-matrix simulations for a given model, including the particle shape distribution, the average equivolume size, and the byproduct particle fraction. The optical fit generates an aspect-ratio distribution of rods in terms of normal distribution, which is compared with the corresponding TEM normal-distribution parameters. Our approach differs from the original method²⁵ in two points. First, we used the depolarization data in addition to the usual extinction spectra. Second, instead of an approximate Gans solution,²⁵ we used the T-matrix method,¹² which allows obtaining an exact and efficient light scattering solution for randomly oriented nonspherical particles.^{10,12} Note that the term "exact" means an accurate solution for Maxwell equations for an exactly defined model determined by its geometrical parameters and material constants. Here, we used the s-cylinder particle shape¹⁰ and a size-corrected dielectric function, as described in detail in refs 26 and 33.

To account for the particle heterogeneity, our models included two particle populations: (1) the major nanorod population and (2) a byproduct particle population with the weight fraction $0 \leq W_b \leq 0.2$. The optical parameters were calculated for both populations and then were summed with the corresponding weights W_b and $W_{\text{rods}} = 1 - W_b$. The nanorod population was modeled by $N = 10$ – 20 fractions of rods possessing a constant thickness $d = 2b$, whereas their aspect ratios were supposed to have normal distribution $\sim \exp[-(p/p_{av} - 1)^2/2\sigma^2]$. The average value p_{av} and the normalized dispersion σ were obtained from TEM data and were also considered fitting parameters for best

agreement between measured and calculated extinction and depolarization spectra. Our computer codes allow efficient computation of the spectral optical properties for distributions of spheroids, right circular cylinders, and circular s-cylinders.

The depolarization ratio Δ_{vh} of randomly oriented particles was calculated by the procedure described in ref 10. Briefly, we first calculated the scattering matrix F_{ij} , which relates the Stokes parameters^{7,12} ($I_{||}$, I_{\perp} , U , V) of the incident and scattered light for an arbitrary oriented particle. The averaging over random orientations was performed as described in ref 27. The normalized scattering matrix element $\langle F_{12} \rangle / \langle F_{22} \rangle$ equaled Δ_{vh} .

From TEM data, we found that the average aspect ratio p_{av} was 3.78 (Figure 5c, inset), the average particle diameter $d = 2b$ was about 15 nm, and the average size of byproduct particles was about 30 nm. For simplicity, the shape of byproduct particles was approximated by spheres, and their weight fraction was considered a fitting parameter close to the TEM observation. Our fitting routine with the extinction and depolarization spectra gave the following best-fitting parameters: $p_{av} = 3.7$ and $W_b = 0.06$. T-matrix calculations with these parameters resulted in excellent agreement between measured and simulated spectra (Figure 5c,d).

Now the question arises: how accurate are the fitting parameters for aspect-ratio distribution and byproduct particles? In agreement with a previous study,²⁵ we found the extinction spectrum fitting to be a very sensitive and versatile tool for determination of the aspect-ratio distribution parameters. Moreover, our fitting procedure takes into account both extinction and depolarization spectra, and it results in more consistent data. This conclusion is supported by the data of Figure 6. Here, we present a comparison of the experimental extinction spectrum with simulations involving variation in the average aspect ratio $p_{av} = 3.6$ and 3.8 at a constant best-fitting value $\sigma = 0.1$, and variation in the dispersion parameter $\sigma = 0.075$ and 0.15 at a constant best-fitting value $p_{av} = 3.7$. These plots show that our fitting generates an aspect-ratio distribution for the rods in solution from which the average aspect-ratio value and its dispersion can be accurately determined. In accord with Eustis and El-Sayed's conclusion,²⁵ we found this approach to be more convenient, robust, and less expensive than the traditional TEM analysis on a solid substrate. Moreover, mindful of the huge number of particles (about 10^{10}) contributing to the optical data, we suppose that the optical fitting is more statistically accurate than the usual TEM distributions based on 500–1000 particles.

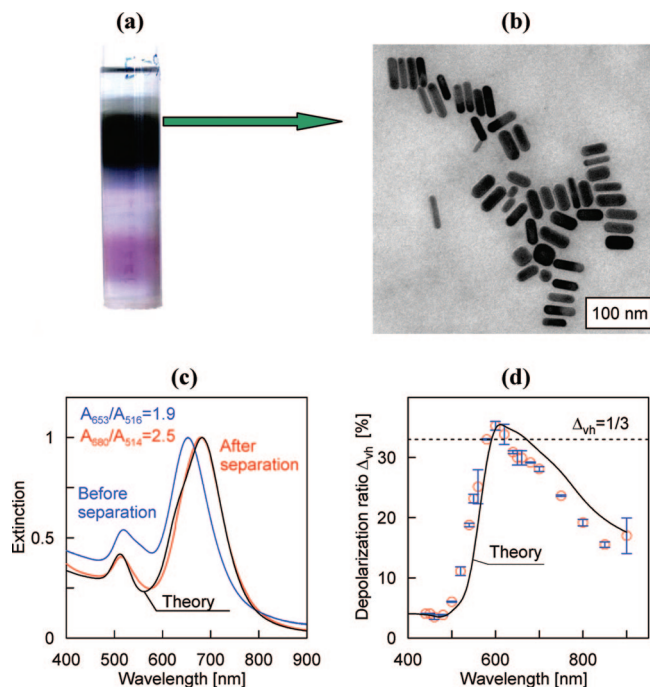


Figure 7. (a) Separation of the NR-670 sample in a stepwise glycerol gradient. (b) TEM image of the upper portion of the first major fraction from the separation tube. (c) Extinction spectra of the NR-670 sample before and after separation, together with T-matrix calculations based on best-fitting data ($p_{av} = 2.8$, $\sigma = 0.1$, $W_b = 0.15$). (d) Experimental and simulated depolarization spectrum. The error bars correspond to three independent runs, with analog and photon-counting data included. The dashed line shows the dielectric-needle limit $1/3$.

3.3. Optical and TEM Characterization of NR-670 and NR-740 Samples. Consider now the experimental and simulated data for the NR-670 sample (Figure 7) with an essentially smaller average aspect ratio $p_{av} = 2.8$ (best fit consistent with the TEM images).

Figure 7b shows a TEM image of particles taken from the upper part of the first separated fraction shown in Figure 7a. Here, in contrast to the plots in Figure 5c, the extinction spectrum of the separated particles is slightly red-shifted, as compared with the nonseparated spectrum. This can be explained by variations in the properties of fractions taken from the upper part of the separated samples. Evidently, this step can involve some uncertainty in the particle-shape and particle-size distributions of a portion taken for the following analysis.

However, more important is the rather low quality of spectra in terms of the peak-extinction ratio, which is less than 3. Keeping in mind this fact and the moderate average aspect ratio $p_{av} = 2.8$, we cannot expect any extra-high depolarization ratios for this sample. Nevertheless, Figure 7d shows a depolarization spectrum with the resonance band values (about 35%) exceeding the dielectric-rod limit $1/3$. Again, such strong depolarization has never been observed with other (e.g., silver²²) colloids. Finally, we note excellent agreement between measured and simulated extinction and depolarization spectra. We omit here all details because they are much similar to those discussed above for the NR-780 sample.

Our final experimental sample, NR-740, was obtained by protocol 2 (with 0.2 M Acros CTAB), which produces nanorods with a “dog-bone”¹⁵ morphology (Figure 8a; the optical properties of such particles have been studied in ref 28). The TEM images also reveal the presence of particles with various morphologies, including “stellated” particles (similar to those observed by Aaron et al.;³ indicated by red arrows in Figure

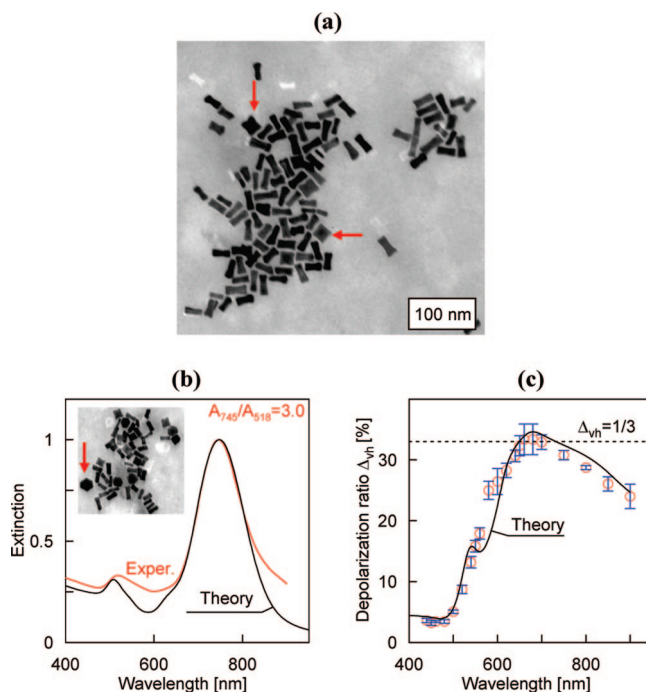


Figure 8. (a) TEM image of a nonseparated NR-740 sample. The red arrows indicate stellated particles (a) and particles with hexagonal symmetry (the inset in panel b). Experimental extinction (b) and depolarization (c) spectra are compared with T-matrix calculations based on TEM data and on the best-fitting model: $p_{av} = 3.4$, $\sigma = 0.11$, $W_b = 0.15$, $p_b = 1.4$, $2b_c = 30$ nm. The error bars correspond to three independent runs with analog and photon-counting data included. The dashed line shows the dielectric-needle limit $1/3$.

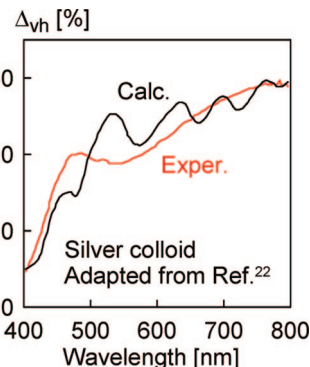


Figure 9. Experimental and simulated depolarization spectra of silver colloids. Recalculated from Figure 4 of ref 22.

8a) and particles with surprising hexagonal symmetry indicated by a red arrow in the inset in Figure 8b.

In agreement with a previous report by Zweifel and Wei,²⁹ we also observed a slight blue-shift temporal trend of the dog-bone-particle plasmon resonance. Besides, we were unable to separate this sample with any significant increase in the peak-extinction ratio. Therefore, the extinction spectrum in Figure 8b and the depolarization spectrum in Figure 8c correspond to the as-prepared solution. The theoretical calculations for this sample were slightly modified to include the effects of stellated particles. Specifically, the byproduct particle fraction was taken as s-cylinders with a small (less than 1.5) aspect ratio p_b . Other fitting details were close to the above examples in Figures 5 and 7. In general, we obtained good agreement between simulated and measured spectra, although the fitting quality was somewhat worse as compared with the NR-780 sample. Again, we observed fairly high, but not outstanding, depolarization

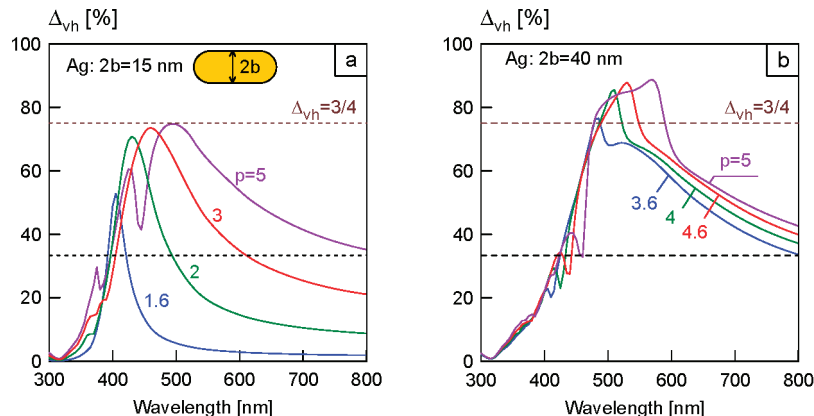


Figure 10. Depolarized light scattering spectra of randomly oriented silver nanorods (s-cylinders) in water. Calculations by the T-matrix method for particle thicknesses of 15 (a) and 40 (b) nm.

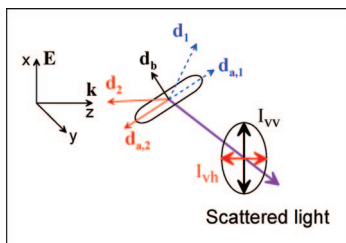


Figure 11. Scheme to explain the physical origin of enhanced depolarization.¹¹ The particle is located in the (x,z) plane. If both (perpendicular and longitudinal) dipoles \mathbf{d}_b and $\mathbf{d}_{a,1}$ oscillate in phase, the direction of the resultant dipole \mathbf{d}_1 is close to the incident electric field \mathbf{E} and the depolarized scattering intensity is small. However, when the dipoles \mathbf{d}_b and $\mathbf{d}_{a,2}$ oscillate out of phase, significant depolarization appears, as the resultant dipole \mathbf{d}_2 is almost parallel to the z -axis.

ratios for this sample. The main result of this experiment is that we did not find any significant difference in depolarization properties between rodlike and dog-bone particles.

3.4. Discussion. In this section, we compare our results with a recent experimental observation of depolarized light scattering from silver colloids.²² In addition, we present T-matrix simulations for silver s-cylinders and briefly discuss the physics behind the unusual depolarization ratio of the plasmon-resonant nanorods. Figure 9 shows the depolarization-ratio spectrum recalculated from plots of anisotropy $(I_{vv} - I_{vh})/(I_{vv} + 2I_{vh}) \equiv (1 - \Delta_{vh})/(1 + 2\Delta_{vh})$ presented in Figure 4 of ref 22. In contrast to our data, the depolarization spectra in Figure 7 show no distinct resonance behavior. Instead, these spectra demonstrate an enhanced long-wavelength depolarization tail. Furthermore, the simulated spectrum shows unexpected oscillations related to particle heterogeneity and, possibly, to the dipolar approximation involved in calculations.²² Thus, it would be desirable to consider first the depolarization properties of silver particles by using an exact electrodynamic basis.

To the best of our knowledge, there have been no exact computations of the depolarized light scattering spectra from silver particles. Here, we present two sets of T-matrix simulations for a simple case of monodisperse silver rods (s-cylinders) with thicknesses $d = 2b = 15$ and 40 nm. For long, thin rods (Figure 10a), multiple resonance spectra related to the multipole plasmon contributions appear.³⁰ However, for small monodisperse and monomorphic particles, we may expect some resonance behavior in depolarized light scattering, analogous to that reported in this work. In agreement with the dipole-approximation analysis,⁹ the upper depolarization ratio limit $3/4$ is confirmed here by an exact simulation presented in Figure 10a. Surprisingly enough, we found that the second dipolar plasmon-

resonant limit $\Delta_{vh} = 3/4$ can be overcome for thick silver nanorods within the 500–600 nm spectral band (Figure 10b). There is no doubt that these resonance properties are related to the multipole plasmon excitations. Of course, the particle size and shape polydispersions will wash out the fine details of the depolarization spectra, whereas the main resonance band should remain.

In conclusion, we discuss the physical mechanisms related to observations of the extra-high depolarization ratio of metal nanorods. For simplicity, we shall treat a small metal nanorod as a dipole particle possessing an axial polarizability tensor $(\alpha_{||}, \alpha_{\perp}, \alpha_{\perp}) \equiv (\alpha_a, \alpha_b, \alpha_b)$, where a and b are the symmetry semiaxis and the perpendicular semiaxis, respectively. A general equation for the depolarization ratio of randomly oriented anisotropic dipole particles^{9,10} can be rewritten as

$$\Delta_{vh} = \frac{\chi^2}{5 - 2\chi^2} \quad (1)$$

$$\chi^2 = \frac{|\alpha_a - \alpha_b|^2}{|\alpha_a|^2 + 2|\alpha_b|^2} \quad (2)$$

The nonnegative quantity χ^2 is always less than $3/2$, so the maximal value of Δ_{vh} equals⁹ $3/4$. From eq 2, the limiting value $\chi^2 = 3/2$ leads to the resonance condition

$$\alpha_a = -2\alpha_b \quad (3)$$

which was obtained in ref 9 for axial particles and was then generalized as $\alpha_a + \alpha_b + \alpha_c = 0$ for the case of $\alpha_b \neq \alpha_c$ in ref 11. Resonance eq 3 elucidates several important physical points. First, it explains the weak dependence of the depolarization maximum on the particle aspect ratio, in drastic contrast with what is observed for the extinction resonance. Indeed, for a very simple spheroidal model, condition 3 leads to the following relationship:⁹

$$\varepsilon = -\gamma\varepsilon_m \quad (4)$$

$$\gamma \equiv \gamma_{vh} = \frac{5 - 3L_a}{3L_a + 1} \quad (5)$$

where ε is the particle dielectric function, ε_m is the dielectric function of the surrounding medium, and L_a is the longitudinal geometrical depolarization factor.^{7,9} Equation 4 has the same form as the well-known condition for the extinction plasmon resonance in spheres (with $\gamma_s = -2$) or nanorods³¹ (with $\gamma_r = L_a^{-1} - 1$). A standard combination of eq 4 with the

Lorentz–Drude formula leads to the plasmon resonance wavelength^{31,32}

$$\lambda_{\text{res}} = \lambda_p [\varepsilon_{\text{ib}} + \gamma \varepsilon_m]^{1/2} \quad (6)$$

where λ_p is the wavelength of electron plasma oscillations and ε_{ib} is the interband contribution to the bulk dielectric function of metal. We now take into account the fact that, for a long rod, $L_a \rightarrow 0$. Accordingly, $\gamma_r \rightarrow \infty$ near the extinction resonance, whereas $\gamma_{\text{vh}} \rightarrow 5$ for the depolarization resonance. Thus, with an increase in the aspect ratio, the extinction resonance wavelength goes to far-infrared, whereas the depolarization resonance wavelength approaches its limiting value

$$\lambda_{\text{res}}^{\text{vh}} = \lambda_p [\varepsilon_{\text{ib}} + 5\varepsilon_m]^{1/2} \approx 610 \text{ nm} \quad (7)$$

where the bulk gold material parameters³³ were used for numerical estimation. Thus, eq 7 qualitatively explains the rather surprising independence of the depolarization resonance wavelength on the particle aspect ratio. Moreover, our estimation for the resonance wavelength (about 610 nm) is in reasonable agreement with the T-matrix simulations and with the experimental observations ($\lambda_{\text{res}}^{\text{vh}} \approx 620 \text{ nm}$).

The second consequence of eq 3 elucidates the physical origin of extra-high depolarization near the resonance. This point has been discussed by Calander et al.,¹¹ so we restrict ourselves to a short comment.

Consider the scattering geometry depicted in Figure 11, in which the incident x -polarized light travels along the positive z -direction and the scattered light is observed in the plane (y, z) in the y -direction. If the particle symmetry axis is directed along the x -, y -, or z -axis, then no depolarization occurs because of evident symmetry constraints. Moreover, no depolarization occurs either for any particle located in the (x, y) or (y, z) plane. Thus, the maximal depolarization contribution is expected from particles located in the (x, z) plane. For usual dielectric rods, the induced dipoles \mathbf{d}_b and $\mathbf{d}_{a,1}$ oscillate in phase. Accordingly, the deviation of the resultant dipole \mathbf{d}_1 from the exciting electric field direction is small. Thus, the depolarized scattering should be weak. However, for metal nanorods, the negative sign in eq 3 means that the perpendicular (\mathbf{d}_b) and longitudinal ($\mathbf{d}_{a,2}$) dipoles are excited in opposite phases.¹¹ In this case, the direction of the resultant dipole \mathbf{d}_2 can be close to the z -axis direction, thus causing the appearance of significant depolarization.

4. Conclusions

To summarize, we have presented unprecedented depolarization spectra of gold nanorods with the resonance maximum between 1/3 and 3/4 theoretical limits established for small dielectric and plasmon-resonant needles, respectively. These experimental observations are in excellent agreement with exact T-matrix simulations based on TEM data for particle sizes and shapes. We have developed a fitting procedure based on simultaneous consideration of the extinction and depolarization spectra. This method gives an aspect-ratio distribution for the rods in solution from which the average value and the standard deviation can be accurately determined in a more convenient and less expensive way than by the traditional TEM analysis. Perhaps our most important result is a set of depolarization spectra for evaluating the quality of a colloid of gold rods prepared in any manner. In some analogy with multipole nanorod extinction spectra,³⁴ the depolarization spectra can be quite informative, including their application to nanobiotechnology, as recently demonstrated in an elegant study by Aaron et al.³ In any case, the presence of an extra-high resonance band

is a signature of a high-quality preparatory procedure that will guide other researchers in determining the homogeneity of their anisotropic particles.

Acknowledgment. This work was partly supported by grants from RFBR (nos. 08-02-00399a, 08-02-01074, and 07-02-01434-a). B.N.K. was supported by grants from the President of the Russian Federation (no. MK 2637.2007.2), INTAS YS Fellowship (no. 06-1000014-6421), the Russian Science Support Foundation, and RFBR (nos. 07-04-00301a and 07-04-00302a).

Supporting Information Available: A short description of the experimental setup for depolarization measurements. This material is available free of charge via the Internet at <http://pubs.acs.org>.

References and Notes

- (1) (a) Sönnichsen, C.; Alivisatos, A. P. *Nano Lett.* **2005**, *5*, 301–304. (b) Nehl, C. L.; Hafner, J. H. *J. Mater. Chem.* **2008**, *18*, 2415–2410.
- (2) Pérez-Juste, J.; Rodríguez-González, B.; Mulvaney, P.; Liz-Marzán, L. M. *Adv. Funct. Mater.* **2005**, *15*, 1065–1071.
- (3) Aaron, J.; de la Rosa, E.; Travis, K.; Harrison, N.; Burt, J.; José-Yacamán, M.; Sokolov, K. *Opt. Express.* **2008**, *16*, 2153–2167.
- (4) (a) Lamprecht, B.; Leitner, A.; Aussenegg, F. R. *Appl. Phys. B: Laser Opt.* **1999**, *68*, 419–423. (b) Canfield, B. K.; Kujala, S.; Laiho, K.; Jefimovs, K.; Turunen, J.; Kauranen, M. *Opt. Express.* **2006**, *14*, 950–955. (c) Sukharev, M.; Sung, J.; Spears, K. G.; Seideman, T. *Phys. Rev. B* **2007**, *76*, 184302. (d) Sung, J.; Sukharev, M.; Hicks, E. M.; Van Deyne, R. P.; Seideman, T.; Spears, K. G. *J. Phys. Chem. C* **2008**, *112*, 3252–3260.
- (5) (a) Stoylov, S. P. *Colloid Electro-Optics: Theory, Techniques, and Applications*; Academic Press: London, 1991. (b) Khlebtsov, N. G.; Melnikov, A. G.; Bogatyrev, V. A. *J. Colloid Interface Sci.* **1991**, *146*, 463–478.
- (6) Kerker, M. *The Scattering of Light and Other Electromagnetic Radiation*; Academic Press: New York, 1969.
- (7) Van de Hulst, H. C. *Light Scattering by Small Particles*; Wiley: New York, 1957.
- (8) Rayleigh, D. W. *Philos. Mag. S. 5* **1871**, *41*, 107–120, 274–279; **1897**, *44*, 28–52.
- (9) Khlebtsov, N. G.; Melnikov, A. G.; Bogatyrev, V. A.; Dykman, L. A.; Alekseeva, A. V.; Trachuk, L. A.; Khlebtsov, B. N. *J. Phys. Chem. B* **2005**, *109*, 13578–13584.
- (10) Alekseeva, A. V.; Bogatyrev, V. A.; Dykman, L. A.; Khlebtsov, B. N.; Trachuk, L. A.; Melnikov, A. G.; Khlebtsov, N. G. *Appl. Opt.* **2005**, *44*, 6285–6295.
- (11) Calander, N.; Gryczynski, I.; Gryczynski, Z. *Chem. Phys. Lett.* **2007**, *434*, 326–330.
- (12) Mishchenko, M. I.; Travis, L. D.; Lacis, A. A. *Scattering, Absorption, and Emission of Light by Small Particles*; Cambridge Univ. Press: Cambridge, U.K., 2002.
- (13) Jana, N. R.; Gearheart, L.; Murphy, C. J. *J. Phys. Chem. B* **2001**, *105*, 4065–4067.
- (14) Nikoobakht, B.; El-Sayed, M. A. *Chem. Mater.* **2003**, *15*, 1957–1962.
- (15) Pissuwan, D.; Valenzuela, S. M.; Killingsworth, M. C.; Xu, X.; Cortie, M. B. *J. Nanopart. Res.* **2007**, *9*, 1109–1124.
- (16) Smith, D. K.; Korgel, B. A. *Langmuir* **2008**, *24*, 644–649.
- (17) Stöber, W.; Fink, A.; Bohn, J. J. *Colloid Interface Sci.* **1968**, *26*, 62–66.
- (18) Khlebtsov, B. N.; Khanadeev, V. A.; Khlebtsov, N. G. *Langmuir*, doi: 10.1021/1a8010053.
- (19) Khlebtsov, N. G.; Bogatyrev, V. A.; Dykman, L. A.; Khlebtsov, B. N.; Krasnov, Ya. M. *J. Quant. Spectrosc. Radiat. Transfer* **2004**, *89*, 133–142.
- (20) Mishchenko, M. I.; Travis, L. D.; Lacis, A. A. *Multiple Scattering of Light by Particles: Radiative Transfer and Coherent Backscattering*; Cambridge Univ. Press: Cambridge, U.K., 2006.
- (21) Gryczynski, Z.; Lukomska, J.; Lakowicz, J. R.; Matveeva, E. G.; Gryczynski, I. *Chem. Phys. Lett.* **2006**, *421*, 189–192.
- (22) Klitgaard, S.; Shtoyko, T.; Calander, N.; Gryczynski, I.; Matveeva, E. G.; Borejdo, J.; Neves-Petersen, M. T.; Petersen, S. B.; Gryczynski, Z. *Chem. Phys. Lett.* **2007**, *443*, 1–5.
- (23) Hanauer, M.; Pierrat, S.; Zins, I.; Lotz, A.; Sönnichsen, C. *Nano Lett.* **2007**, *7*, 2881–2885.
- (24) Jiang, X. C.; Brioude, A.; Pileni, M. P. *Colloids Surf., A* **2006**, *277*, 201–206.
- (25) Eustis, S.; El-Sayed, M. A. *J. Appl. Phys.* **2006**, *100*, 044324.
- (26) Khlebtsov, B. N.; Khlebtsov, N. G. *J. Biomed. Opt.* **2006**, *11*, 04402.

- (27) Khlebtsov, N. G.; Melnikov, A. G. *Opt. Spectrosc.* **1995**, *79*, 605–609.
- (28) Xu, X.; Cortie, M. B. *Adv. Funct. Mater.* **2006**, *16*, 2170–2176.
- (29) Zweifel, D. A.; Wei, A. *Chem. Mater.* **2005**, *17*, 4256–4261.
- (30) Khelbtsov, B. N.; Khlebtsov, N. G. *J. Phys. Chem. C* **2007**, *111*, 11516–11527.
- (31) Kelly, K. L.; Coronado, E.; Zhao, L. L.; Schatz, G. C. *J. Phys. Chem. B* **2003**, *107*, 668–677.
- (32) Khlebtsov, N. G.; Trachuk, L. A.; Mel'nikov, A. G. *Opt. Spectrosc.* **2005**, *98*, 77–83.
- (33) Khlebtsov, N. G.; Bogatyrev, V. A.; Dykman, L. A.; Melnikov, A. G. *J. Colloid Interface Sci.* **1996**, *180*, 436–445.
- (34) Payne, E. K.; Shuford, K. L.; Park, S.; Schatz, G. C.; Mirkin, C. A. *J. Phys. Chem. B* **2006**, *110*, 2150–2154.

JP802874X